

Effects of silanol defects and Ti site location within Ti-MWW on alkene epoxidation with aqueous hydrogen peroxide

Ohsung Kwon^a, David S. Potts^a, David W. Flaherty^{a,b,*}

^a Department of Chemical and Biomolecular Engineering, University of Illinois Urbana-Champaign, Urbana, IL 61801, USA

^b School of Chemical and Biomolecular Engineering, Georgia Institute of Technology, Atlanta, GA 30332, USA



ARTICLE INFO

Keywords:

Zeolite
Selective oxidation
Defect engineering
Active site location
Hydrothermal synthesis

ABSTRACT

Catalytic reaction kinetics and thermodynamics within zeolites respond to the physical properties of the framework through noncovalent interactions with solvents. Here, we demonstrate that rates of alkene epoxidations depend sensitively upon the topological location of Ti atoms and the density of silanol ($(\text{SiOH})_x$) defects in hydrothermally synthesized Ti-MWW catalysts. Turnover rates for 1-hexene epoxidation do not change systematically with $(\text{SiOH})_x$ density unlike previous reports for other zeolite framework. Site-averaged turnover rates on Ti-MWW catalysts with the greatest portion of Ti sites located in sinusoidal channels exceed those on materials with most Ti in supercages by a factor of 40-fold. These differences appear to reflect free energy contributions and compensation between activation enthalpies and entropies, induced by the structural organization of solvent molecules that responds differently to the topological locations of active sites and the presence of defects.

1. Introduction

Catalytic epoxidations of alkenes with hydrogen peroxide (H_2O_2) over microporous titanosilicate catalysts attracts both industrial and academic interests, because these reaction possess lower environmental impact than previous epoxide formation methods [1,2]. Million tons of propylene oxide (1,2-epoxypropane) are currently synthesized with titanosilicates and H_2O_2 using the hydrogen peroxide-propylene oxide (HPPO) process [3–6]. Zeolites of the MFI topology and containing framework substituted Ti atoms are widely used in this process with methanol as a solvent, as well as for other chemistries including ketone ammoniation [7–9]. Following the commercialization of the first generation Ti-MFI catalytic system, a second generation HPPO was introduced which uses Ti-MWW catalysts with H_2O_2 in the presence of acetonitrile (CH_3CN), which is an aprotic solvent [10–14]. Notably, the presence of solvent molecules condensed near active sites alters the stability of reactive species for alkene epoxidations, among other reactions, through noncovalent interactions that significantly influence turnover rates [15]. Recent studies highlighted these phenomena and sought to quantify the contributions of noncovalent interactions between pore, solvent, and reactive intermediates to excess activation free energies ($\Delta G^{\ddagger,\epsilon}$) that reflect the thermodynamic non-ideality to

reactants and transition states and stabilize the catalytic reactions in different magnitudes, adding to the standard activation free energy ($\Delta G^{\ddagger,0}$) [16–22], as described in Eq. 1.

$$\Delta G^\ddagger = \Delta G^{\ddagger,0} + \Delta G^{\ddagger,\epsilon} \quad (1)$$

These excess contributions appear to reflect changes in the structural organization of solvent and reactant molecules within the vicinity of the active site, and their magnitude and changes in catalytic rates depend on the pore polarity, topology, solvent identity, or even quantity of solvent molecules near active sites. Di Iorio *et al.* demonstrated greater hydrogen transfer turnover rates over defect-free BEA zeolites with Sn sites compared to the BEA zeolites that also contained $(\text{SiOH})_x$ defects, due to the stabilization of transition states within ordered solvent networks [22]. Glucose isomerization catalyzed with Ti-BEA catalysts shows up to a 10-fold increase in reaction rates with a $(\text{SiOH})_x$ -free Ti-BEA, as well as a more stabilized transition state than $(\text{SiOH})_x$ -dense Ti-BEA due to the absence of intrapore H_2O molecules [21]. Comparisons between alkene epoxidation kinetics with Ti-zeolites with distinct topologies (MFI, BEA, and FAU) and controlled $(\text{SiOH})_x$ densities revealed the crucial role of solvent-mediated interactions among reactive intermediates and the extended structure of zeolite pores, which yield greater turnover rates that are orders of magnitude greater over $(\text{SiOH})_x$ -dense pores than

* Corresponding author at: Department of Chemical and Biomolecular Engineering, University of Illinois Urbana-Champaign, Urbana, IL 61801, USA.
E-mail address: dflaherty3@gatech.edu (D.W. Flaherty).

defect free pores caused by differences in $\Delta G^{\ddagger,e}$ [16–20]. Taken together, the physical properties of microporous catalyst materials and the organization of solvent and reactive intermediates can significantly affect catalytic performances.

The topological location of catalytically active sites in titanosilicate materials significantly influences catalytic rates and selectivity, depending on the reaction conditions (e.g., zeolite species, substrate size, and pore diameters) [23–29]. The framework of MWW possesses tetrahedral sites in 12-membered supercages (0.71–1.82 nm), 12-membered side pockets, and 10-membered sinusoidal channels (0.4–0.55 nm), and these large differences among characteristic void dimensions differ considerably from the more uniform voids in other materials (e.g., MFI, *BEA, FAU) [30]. Incorporated heteroatoms that catalyze alkene epoxidations (e.g., Ti) reside at the tetrahedral position and are not uniformly sited within the MWW structure [31]. Studies have shown that the heterogeneity among the positions of Ti active sites directly impacts rates and selectivities for Ti-MWW catalyzed reactions [14,29,32]. For example, the epoxidation of cyclohexene with *tert*-butyl hydroperoxide was reported to occur only at Ti sites located within the larger 12-membered side pockets and supercages due to the bulkiness of the reactive intermediate and their inability to organize to form transition states for oxygen transfer within sinusoidal channels [29]. By selectively blocking Ti sites in supercages of Ti-MWW with triphenylamine, Wu *et al.* demonstrated that the epoxidation of allyl alcohol occurs at Ti sites in sinusoidal channels of Ti-MWW [14]. Similar approaches were used to show that 1-pentene epoxidizes predominantly at Ti sites within sinusoidal channels [32]. Most recently, Grossi-Giordano *et al.* showed that the entropic factors lead to higher cyclohexene epoxidation rates with *tert*-butyl hydroperoxide at Ti sites inside 12-membered pockets located on the exterior of *-SVY topology over reactions within sinusoidal channels [33]. These findings indicate that the epoxidation kinetics at Ti sites located in various pores vary depending on the dimension and bulkiness of alkene substrates and the hydroperoxide coreagent. Prior kinetic measurements after post-synthetic modifications or additions of heteroatoms to control the Ti-MWW pore hydrophobicity were conducted at high reactant conversions and often with the presence of residual heteroatoms (e.g., fluorine), and as such, these earlier report do not describe the effects of solvent molecules, Ti atom location, or $(\text{SiOH})_x$ defects on site specific turnover rates or kinetic barriers [34–36].

Several groups have reported the effects of reduced hydrophilicity on apparent rates and selectivities for alkene epoxidations by structurally modifying the Ti-MWW framework. Introducing ethanol to rinse out organic precursors during syntheses of Ti-MWW led to lower defect densities and higher conversions of C_6H_{12} [34]. Adding post-synthetic modification such as amine treatment (e.g., piperidine and hexamethyleneimine) [35], implanting fluorine species [36–39], substituting $(\text{SiOH})_x$ defects to trimethylsilyl species ($-\text{Si}(\text{CH}_3)_3$) [40], and changing acid treatment time after the crystallization of MWW framework [41] resulted in the reduced densities of $(\text{SiOH})_x$ defects and greater conversions of alkenes by epoxidation reactions over Ti-MWW catalysts. In contrast, the intrapore $(\text{SiOH})_x$ defect density of zeolites may be controlled through combinations of post-synthetic modifications and hydrothermal synthesis within fluoride media, which impact rates and selectivities for alkene epoxidations significantly [16,17,19,20,42–45]. Prior studies demonstrated that the disruption of solvent networks (i.e., hydrogen bonded mixtures of H_2O and CH_3CN) to accommodate the formation of transition states in zeotype materials leads to more positive apparent activation energy ($\Delta S^{\ddagger,e}$) for epoxidation of 1-octene (and other alkenes), which results in a 100-fold increase in turnover rates over $(\text{SiOH})_x$ -dense Ti-BEA [17]. The apparent contradictions between the concepts described in these earlier studies imply that more extensive studies of the influence of synthesis methods and the $(\text{SiOH})_x$ density in Ti-MWW on alkene epoxidation are needed to understand how these factors impact kinetics and the reasons behind apparent differences among rates and barriers for these materials.

Here, we report C_6H_{12} epoxidation kinetics with H_2O_2 over a series of Ti-MWW catalysts with varying crystallographic locations of Ti active sites and densities of intrapore $(\text{SiOH})_x$ defects. We develop hydrothermal synthesis methods of Ti-MWW catalysts to control the number of $(\text{SiOH})_x$ defects within proximity to Ti sites by controlling the contents of additives during crystallization (boric acid (H_3BO_3) and hydrofluoric acid (HF)), and we utilize common hydrothermal synthesis methods to vary Ti contents for the purpose of changing the topological location of Ti active sites. With these synthesized catalysts, we explain how consequential differences in rates and activation barriers for C_6H_{12} epoxidation reflect changes in interactions among solvent molecules, pore $(\text{SiOH})_x$ defects, and reactive species near active sites.

2. Materials and methods

2.1. Synthesis of Ti-MWW catalyst

Ti-MWW catalysts were hydrothermally synthesized with varying structure directing agents (SDA), by following previously reported synthesis methods [46,47]. Ti-MWW-B(*a*; *a* depicts the atomic ratio of Si to B in the synthesis gel) catalysts were synthesized hydrothermally with fumed silica (SiO_2 ; Cabot, CAB-O-SIL M-5), boric acid (Sigma-Aldrich, 99.5%), titanium butoxide (TBOT; Sigma-Aldrich, 97%, reagent grade), deionized (DI) H_2O (18.2 $\text{M}\Omega\cdot\text{cm}$, Elga Purelab Flex 2) and piperidine (PI; Sigma-Aldrich, 99%) as an SDA. Molar ratios of 1 Si: *a* B: 0.01 or 0.02 Ti: 0.2 PI: 10 H_2O were introduced for the synthesis gel. For example, to synthesize Ti-MWW-B(0.5) with a Si to Ti ratio of 100, PI (30.3 g) was dissolved in DI H_2O (86.90 cm^3) in a polypropylene container with a screw cap. This mixture solution was divided into two equal solutions, TBOT (0.86 g) was put into one solution, and 31.42 g of H_3BO_3 was added to the other solution. These solutions were stirred for 30 min in room temperature to hydrolyze TBOT completely. SiO_2 (7.63 g) was put into each solution, and the two solutions were magnetically stirred for 1 h (160 rpm, 298 K). Then the two solutions were combined and stirred for 1 h to produce a homogeneous opaque white solution. This solution was transferred to a Teflon-lined stainless steel autoclave (Parr, 4744 and 4748) with a small amount of previously synthesized Ti-MWW-B particles (2% by mass of SiO_2), and heated to 423 K in a convection oven (Yamato, DKN602C) for 13 days. Ti-MWW-F (*b*; *b* equals to molar ratio of HF to the SDA (trimethyladamantylammonium hydroxide, TMAdaOH)) added to the synthesis gel) catalysts were synthesized hydrothermally with fumed SiO_2 , potassium carbonate (K_2CO_3 ; Sigma-Aldrich, 99.995%, trace metal basis), DI H_2O , and hexamethyleneimine (HMI; Sigma-Aldrich, 99%) and TMAdaOH (Sachem, 25% in H_2O) as SDAs with adding various amounts of HF. Gel mixtures of 1 Si: 0.01 or 0.02 Ti: 0.14 K: 0.3 HMI: 0.2 TMAdaOH were used for the synthesis. For example, to synthesize Ti-MWW-F(0) with a Si to Ti ratio of 100, HMI (3.66 cm^3) and TMAdaOH (17.26 cm^3) were dissolved in DI H_2O (51.45 cm^3), and the solution was divided into two solutions of equal volume. TBOT (0.38 g) was added to one solution, and K_2CO_3 (1.05 g) was added to the other solution. After stirring for 30 min, SiO_2 (3.22 g) was introduced to each solution, and the solutions were stirred for 1 h. Subsequently, the two solutions were combined and mixed for 1 h and then transferred to a Teflon-lined stainless steel autoclave (Parr, 4744 and 4748). Varying amounts of HF ($\text{HF:TMAdaOH} = b$, where $0 \leq b \leq 0.5$) were added to the synthesis gel in the Teflon liner, and the gel was stirred manually with a polypropylene spatula in the presence of a previously synthesized Ti-MWW-F seed (2% by mass of SiO_2). The resulting gel was then heated to 413 K in a convection oven (Yamato, DKN602C) within continuously rotating autoclaves (60 rpm) for 11 days.

After the thermal treatment steps, crystallized Ti-MWW-B and Ti-MWW-F precipitates exhibiting yellow colors were recovered with centrifugation (10,000 rpm, 10 min) and rinsed with DI H_2O ($50 \text{ cm}^3 \cdot \text{g}^{-1}$ zeolite). Each precipitate was rinsed with DI H_2O three times. The wet solids recovered by centrifugation were dried in a convection

oven at 348 K for 1 day. The dry powders were treated with 2 M nitric acid (HNO_3 ; Macron, 70%, $20 \text{ cm}^3 \cdot \text{g}^{-1}$ zeolite) at 373 K for 1 day to etch the remaining B and K species inside the MWW framework for Ti-MWW-B and Ti-MWW-F, respectively. The treated solids were recovered by vacuum filtration, loaded into a quartz boat, and then calcined within a three-zone horizontal furnace (Applied Test Systems, 3210) by heating from ambient temperature to 823 K at a linear rate of $5 \text{ K} \cdot \text{min}^{-1}$ and holding at 873 K for 6 h within flowing dry air (Airgas, Ultra Zero Grade, $100 \text{ cm}^3 \cdot \text{min}^{-1}$) to remove moisture and organic residues, such as SDA, from the zeolite framework.

2.2. Characterization of synthesized catalysts

Zeolite crystallinities of synthesized Ti-MWW-B and Ti-MWW-F powders were analyzed via an X-ray diffractometer (Bruker, D8 advance) with Cu K α radiation (0.15418 nm) on a polypropylene holder under the ambient condition.

Ti contents in all Ti-MWW catalysts and K contents in Ti-MWW-F were measured with an energy-dispersive X-ray fluorescence spectrometer (EDXRF; Shimazu, EDX-7000). Powder samples were ground, loaded in a sample holder (1 cm diameter), sealed with an Ultralene film, and placed into the sample chamber purged with He during analyses in ambient temperature and pressure conditions. The quantity of boron within Ti-MWW-B was measured via an inductively coupled plasma optical emission spectrometer (ICP-OES; PerkinElmer, Optima 8300), which was pre-calibrated with diluted standards.

Diffuse reflectance ultraviolet-visible (DRUV-Vis) spectra were collected on a spectrometer (Agilent, CARY 5) equipped with a diffuse reflectance accessory (Harrick, Cricket) and were used to estimate the dispersity of Ti atoms in the MWW framework. The catalyst samples were mixed with MgO (Sigma-Aldrich, 99.995%) at a 1:10 ratio by mass before the analyses and put into the reflectance accessory attached to the spectrometer. The reflectance spectra were obtained between 200 and 800 nm under ambient conditions. For the total reflectance, a pure MgO sample was used as the background. Tauc plots were constructed and used to calculate the band gap energies of these materials by extrapolating linear regions of the Kubelka-Munk functions to the abscissa (detailed calculations are shown in [Supporting Information](#) (Section S1.2)).

A Fourier-transform infrared spectrometer (Bruker, Vertex 70) with a HgCdTe detector (cooled with liquid nitrogen) was used to measure relative $(\text{SiOH})_x$ densities in synthesized catalysts. The cell was heated to 573 K (at the ramp rate of $5 \text{ K} \cdot \text{min}^{-1}$) with a temperature controller (Watlow, EZ-Zone). Background absorbance spectra (128 scans, 1 cm^{-1} resolution) were taken at 573 K under He flow (Airgas, Ultra High Purity, $10 \text{ cm}^3 \cdot \text{min}^{-1}$). The gas flow rate was controlled by a digital mass flow controller (Alicat, MC-Series) within a gas manifold. Before the measurement, a background spectrum was taken with an empty transmission cell with two CaF_2 windows and two stainless steel alignment rings (573 K, 101 kPa He) [19]. After the background measurement, Ti-MWW samples ($\sim 50 \text{ mg}$) were pressed into a self-supporting disk of 2 cm diameter with a hydraulic press (Carver, Model C), and loaded into the transmission cell. The cell was then heated to 573 K for 1.5 h under He flow to remove the remaining H_2O and volatile species inside the zeolite framework. Absorbance spectra of Ti-MWW samples were then measured (128 scans, 1 cm^{-1} resolution).

Measured uptakes from solutions of *(1 R, 2 R)-(+)-1,2-diphenylethylenediamine* (DPED; Sigma-Aldrich, 97%) in contact with Ti-MWW materials were conducted to specify Ti active site locations in synthesized catalysts. Ti-MWW ($\sim 30 \text{ mg}$) was added to a 10 cm^3 solution of CH_3CN (Fisher Chemical, HPLC grade) solvent containing a trace amount of benzene (Sigma-Aldrich, analytical standard grade) as an internal standard, and DPED with a molar ratio of DPED to Ti atoms of 1.4. The solutions were stirred for 30 min at 313 K after adding the catalyst. Aliquots of the solutions were taken before and after adding catalysts using a 1 mL plastic syringe (Covidien, Monoject Tuberculin),

and filtered with a $0.22 \mu\text{m}$ syringe filter (Tisch Scientific, SF14704) to remove solid catalyst particles. The chemical composition of the solutions was determined with a gas chromatograph with a flame ionization detector (GC-FID; Agilent, 6890) and a capillary column (Agilent, HP-1; 50 m length, $320 \mu\text{m}$ inner diameter, $1.05 \mu\text{m}$ inner film).

2.3. Turnover rate measurements for 1-hexene epoxidation

Batch reactions for the C_6H_{12} epoxidation with H_2O_2 over synthesized Ti-MWW catalysts were conducted in round-bottom flasks with reflux condensers. The liquid phase (30 cm^3) consisted of CH_3CN solvent, 5–50 mM H_2O_2 with 19.5–195 mM H_2O (Macron Fine Chemicals, 30% in H_2O), 0.1–20 mM C_6H_{12} (Sigma-Aldrich, $\geq 99\%$), and a trace amount of benzene (Sigma-Aldrich, analytical standard grade) as an internal standard. Batch reactors were heated to the desired temperature (303–333 K) and kept stirring for 30 min on heating plates (Corning, PC-420D) with Teflon magnetic stirring bars. An initial aliquot (0.5 cm^3) of the solution was taken to confirm the starting composition of the liquid-phase, and then Ti-MWW ($\sim 20 \text{ mg}$) was added to initiate the reaction. Aliquots of solutions (0.5 cm^3) were extracted at 5 min intervals using a 1 cm^3 plastic syringe (Covidien, Monoject Tuberculin) and filtered with a $0.22 \mu\text{m}$ syringe filter (Tisch Scientific, SF14704) to terminate further reactions by removing solid catalysts. The composition of the reaction solution was analyzed using a gas chromatograph (GC, Agilent, 6890) equipped with a flame ionization detector and a capillary column (Agilent, HP-1; 50 m length, $320 \mu\text{m}$ inner diameter, $1.05 \mu\text{m}$ inner film). Initial product formation rates were calculated from quadratic fits to concentrations measured as functions of time, using only data points collected when the conversion of C_6H_{12} was below 5% (differential conversion regime) in order to minimize the influence of product inhibition and reactant depletion on reported rates.

In situ site titration experiments were performed by adding titrants ethylenediamine (ED; Sigma-Aldrich, 99%) or DPED (Sigma-Aldrich, 97%) with molar ratios of titrants to Ti atoms extending from zero to two. Titrants were added to the reaction mixtures (30 cm^3) containing 2 mM C_6H_{12} , a trace amount of benzene (internal standard), and Ti-MWW ($\sim 20 \text{ mg}$) in CH_3CN . Solutions were stirred for 30 min at 313 K to allow the titrants to bind to Ti sites. In these experiments, the reaction was initiated by adding 0.03 cm^3 of aqueous H_2O_2 solution (Macron Fine Chemicals, 30% in H_2O) to keep the concentration of H_2O_2 and H_2O to 10 mM and 39 mM, respectively, and subsequently, aliquots of solutions (0.5 cm^3) were taken at 5 min intervals, filtered, and analyzed via GC-FID.

3. Results and discussion

3.1. Synthesis results of Ti-MWW catalysts with varying silanol density and Ti site location

Ti-MWW-B and Ti-MWW-F catalysts were hydrothermally synthesized with the intent to vary $(\text{SiOH})_x$ densities and topological locations of Ti atoms inside the MWW zeolite framework. Previously, $(\text{SiOH})_x$ defects were created by chemically etching framework B-atoms from samples synthesized with H_3BO_3 [48]. Thus, we synthesized Ti-MWW-B catalysts within increasing numbers of framework B by adding increasing amounts of H_3BO_3 ($0.5 \leq \text{Si:B} \leq 1.5$) to the synthesis gel, and subsequently, converting framework B atom into $(\text{SiOH})_x$ groups by immersing in aqueous HNO_3 (2 M HNO_3 , at 373 K for 1 day). In addition, we created Ti-MWW-F materials that possess lower densities of $(\text{SiOH})_x$ by synthesis involving two SDAs (hexamethyleneimine and TMAdaOH) [46,49] with the addition of HF ($0 \leq \text{HF:TMAdaOH} \leq 0.5$). The association of fluoride anions with the organic cations of the SDA within the gel leads to a reduction in resulting $(\text{SiOH})_x$ groups: greater molar ratios of HF to SDA lead to lower $(\text{SiOH})_x$ densities for MFI and *BEA zeolites among others [16,21,50,51]. Here, HF was added to synthesis gels with the intent of reducing the densities of $(\text{SiOH})_x$ within

a series of Ti-MWW-F materials. To distinguish among these synthesis approaches, materials are denoted as either Ti-MWW-B(x) or Ti-MWW-F(y), where x and y are the molar ratios of Si to B or HF to TMAdaOH, respectively.

Fig. 1 shows X-ray diffraction (XRD) patterns of synthesized Ti-MWW-B (**Fig. 1a**; Si:Ti = 100 and $0.5 \leq \text{Si:B} \leq 1.5$) and Ti-MWW-F (**Fig. 1b**; Si:Ti = 50 and $0 \leq \text{HF:TMAdaOH} \leq 0.5$) catalysts. Diffractograms for Ti-MWW catalysts with other synthesis conditions appear in the *Supplementary Information* (**Fig. S1**). The XRD patterns of these materials match those for crystalline MWW zeolites [47], which indicates the successful crystallization of this structure by both methods. Ti-MWW-B samples with atomic ratios of Si to B less than 0.5 or greater than 1.5 and Ti-MWW-F samples with molar ratios of HF to TMAdaOH greater than 0.5 did not exhibit diffraction features consistent with the MWW structure, even after an extended period of crystallization over 40 days, resulting in amorphous structures. Heteroatom contents (B and K for Ti-MWW-B and Ti-MWW-F, respectively) estimated via EDXRF and ICP-OES data in **Table 1** show that acid treatments with 2 M HNO_3 remove remaining heteroatoms within MWW framework. Calculated band gap energies of all synthesized Ti-MWW catalysts fall within the range of 3.7–4.3 eV (**Table 1**) with a single feature absorption peak near 5.2 eV (220 nm, **Fig. S2**), regardless of Ti contents ($50 \leq \text{Si:Ti} \leq 200$) [52,53]. These band gap energies are greater than for anatase titanium dioxide (TiO_2 ; 3.2 eV) and imply that the Ti atoms are highly dispersed throughout the MWW framework, regardless of the choice of synthesis methods or compositions.

Infrared spectra of dehydrated zeolite powders provide one semi-quantitative method to compare densities of $(\text{SiOH})_x$ defects between Ti-MWW materials. **Fig. 2** shows normalized infrared spectra of Ti-MWW-B and Ti-MWW-F, respectively, following thermal treatments intended to remove residual water (101 kPa He, 573 K, 1.5 h). **Figure S3** presents infrared spectra for all the other Ti-MWW catalysts. Broad absorbance features between 3200 and 3800 cm^{-1} represent $\nu(\text{O-H})$ features of $(\text{SiOH})_x$ defects distinguished by the extent of hydrogen bonding interactions, and features at 1870 cm^{-1} and 1990 cm^{-1} represent $\nu(\text{Si-O-Si})$ overtones of the MWW framework [16,54]. Absorbances normalized by the intensity of the framework vibration at 1870 cm^{-1} allow for direct comparisons between the peak areas of $\nu(\text{O-H})$ features ($A_{\nu(\text{O-H})}$) among samples. Visual comparisons among $A_{\nu(\text{O-H})}$ from normalized spectra indicate that densities of $(\text{SiOH})_x$ defects decrease as the Si to B ratio increases (**Fig. 2a**) and as the HF to TMAdaOH ratio

increases (**Fig. 2b**).

A more precise comparison of these $(\text{SiOH})_x$ densities across Ti-MWW samples derives from calculations for a unitless parameter (ϕ_{IR}), shown in **Eq. 2**

$$\phi_{\text{IR}} = \frac{A_{\nu(\text{O-H})}}{A_{\nu(\text{Si-O-Si})}} \quad (2)$$

where $A_{\nu(\text{O-H})}$ represents the areas of the bimodal peaks for hydrogen-bonded $\nu(\text{O-H})$ features (3680 cm^{-1} and 3540 cm^{-1} of $(\text{SiOH})_x$ nests). Sharp peaks at 3750 cm^{-1} in **Fig. 2** are associated with isolated SiOH groups, located in the external surface of MWW structures [16,55]. These isolated SiOH groups would not interact strongly with reactive species or solvents near active sites; thus, we excluded these sharp features in $A_{\nu(\text{O-H})}$ and following discussions of the effects of $(\text{SiOH})_x$ defects on reaction kinetics. The variable $A_{\nu(\text{Si-O-Si})}$ signifies the combined peak area of $\nu(\text{Si-O-Si})$ overtones at 1870 cm^{-1} and 1990 cm^{-1} , which serves as a measure of the quantity of zeolite within the beam path [56].

Fig. 3 shows that values of ϕ_{IR} values for synthesized Ti-MWW materials decrease with increasing ratios of Si to B ratios (**Fig. 3a**) and HF to TMAdaOH (**Fig. 3b**), regardless of Ti contents. Values of ϕ_{IR} for Ti-MWW-B decrease by 4-fold decrease when the Si/B ratio increases from 0.5 ($\phi_{\text{IR}} = 4.0$) to 1.5 ($\phi_{\text{IR}} = 0.9$), which agrees with the expected formation of $(\text{SiOH})_x$ defects after etching framework B atoms with HNO_3 [48]. Similarly, ϕ_{IR} values for Ti-MWW-F materials decrease systematically and differ by a factor of two as the HF to TMAdaOH ratio increases from 0 to 0.5. This trend indicates that the presence of fluoride during hydrothermal synthesis suppresses the formation of $(\text{SiOH})_x$ defects within the MWW framework, consistent with prior observations for Lewis acidic MFI and *BEA zeolites [21,50,51]. Error bars depict standard deviations of ϕ_{IR} values among Ti-MWW-B (**Fig. 3a**) and Ti-MWW-F (**Fig. 3b**) catalysts that have identical Si to B or HF to TMAdaOH ratios. Among these groups, the samples are differentiated by the atomic ratios of Si to Ti varied from 50 to 200 for Ti-MWW-B and from 50 to 100 for Ti-MWW-F. These lesser differences in values of ϕ_{IR} (below 12%) across various Si to Ti ratios indicate that this collection of synthesis methods provides control over the $(\text{SiOH})_x$ density in pores independent from the Ti content of the final material.

These observations demonstrate that the density of $(\text{SiOH})_x$ defect sites can be varied by approximately a factor of four and depends upon the quantity of H_3BO_3 or HF included during the synthesis of Ti-MWW. Although the span of ϕ_{IR} values overlaps for these two synthesis

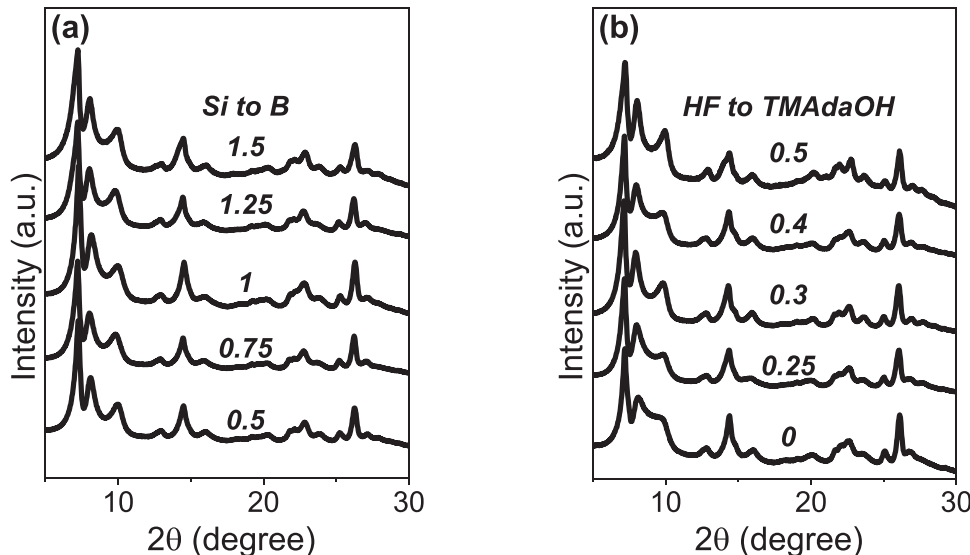


Fig. 1. X-ray diffractograms for representative Ti-MWW materials including (a) Ti-MWW-B(x) with varying ratios of Si to B ($x = 0.5, 0.75, 1.0, 1.25, 1.5$; Si:Ti = 100), and (b) Ti-MWW-F(y) with varying molar ratios of HF to TMAdaOH ($y = 0, 0.25, 0.3, 0.4, 0.5$; Si:Ti = 50). All diffraction patterns are normalized by the peak at 7.2 degree and offset for clarity.

Table 1

Composition and Physical Characteristics of Ti-MWW Materials after Wet Chemical and Thermal Treatments. Values include molar ratios of Si to Ti, Si to B (Ti-MWW-B) or HF to TMAdaOH (Ti-MWW-F) in the synthesis gel, synthesis times (days), contents of Ti and B (Ti-MWW-B) or K (Ti-MWW-F) in the oxidatively treated materials (wt%), band gap energies (eV), relative $(\text{SiOH})_x$ densities (ϕ_{IR}), and estimated fractions of Ti sites in sinusoidal channels (χ_{sinusoid}) within Ti-MWW-B and Ti-MWW-F.

Sample name	Synthesis Parameters			Characteristics of Oxidatively Treated Materials				
	Initial Si to Ti ratio	Si to B or HF to TMAdaOH ratio	Synthesis time (day)	Ti content (wt %) ^a	B or K content (wt %) ^b	Band gap energy (eV) ^c	$\phi_{\text{IR}}^{\text{d}}$	$\chi_{\text{sinusoid}}^{\text{e}}$
Ti-MWW-B (0.5)	100	0.5	13	0.41	0.27	4.15	4.0	0.21
Ti-MWW-B (0.75)	100	0.75	13	0.34	0.23	4.26	3.3	0.34
Ti-MWW-B (1.0)	50	1.0	13	0.84	0.28	3.70	3.2	0.63
Ti-MWW-B (1.0)	100	1.0	13	0.37	0.32	4.27	2.8	0.28
Ti-MWW-B (1.0)	150	1.0	13	0.24	0.23	4.13	3.6	0.12
Ti-MWW-B (1.0)	200	1.0	13	0.18	0.22	4.16	2.9	0.04
Ti-MWW-B (1.25)	100	1.25	13	0.23	0.16	4.25	2.4	0.07
Ti-MWW-B (1.5)	100	1.5	13	0.38	0.19	4.00	0.9	0.13
Ti-MWW-F(0)	50	0	11	1.55	0.02	3.94	2.1	0.73
Ti-MWW-F(0)	100	0	11	0.62	0	3.82	2.0	0.48
Ti-MWW-F (0.1)	100	0.1	11	0.46	0	4.09	1.5	0.24
Ti-MWW-F (0.2)	100	0.2	11	0.41	0	4.10	1.5	0.40
Ti-MWW-F (0.25)	50	0.25	11	1.05	0	4.26	1.6	0.76
Ti-MWW-F (0.3)	50	0.3	11	0.96	0	4.27	1.4	0.52
Ti-MWW-F (0.4)	50	0.4	11	1.07	0.01	4.11	1.3	0.64
Ti-MWW-F (0.5)	50	0.5	11	1.28	0.04	4.02	1.3	0.85
Ti-MWW-F (0.5)	100	0.5	11	0.59	0	4.03	1.1	0.41

^a Measured using EDXRF.

^b Measured using ICP-OES (B) and EDXRF (K).

^c Measured using DRUV-Vis.

^d Calculated by infrared spectroscopy.

^e Estimated by uptake measurement with (1 R,2 R)-(+) -1,2-diphenylethylenediamine.

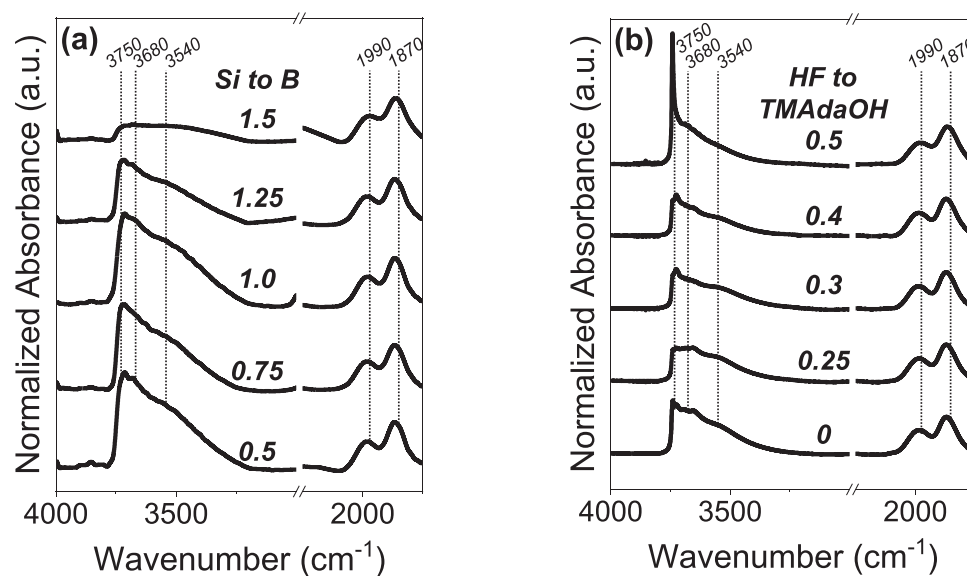


Fig. 2. Normalized infrared spectra for (a) Ti-MWW-B(x) with varying ratios of Si to B ($x = 0.5, 0.75, 1.0, 1.25, 1.5$; Si:Ti = 100) and (b) Ti-MWW-F(y) with varying molar ratios of HF to TMAdaOH ($y = 0, 0.25, 0.3, 0.4, 0.5$; Si:Ti = 50) (101 kPa He, 573 K). All spectra are normalized to the $\nu(\text{Si}-\text{O}-\text{Si})$ feature (1870 cm^{-1}) and are vertically offset for clarity.

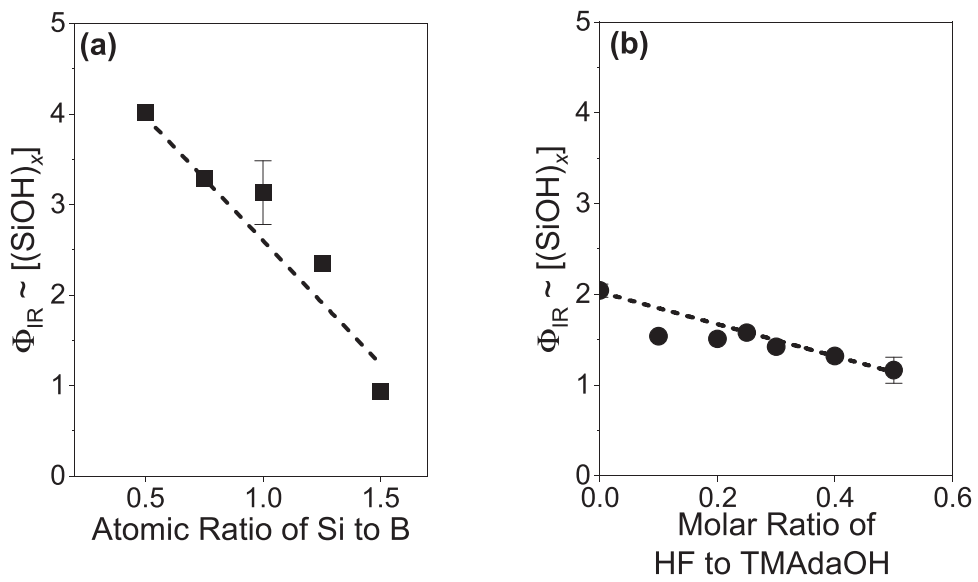


Fig. 3. Values of ϕ_{IR} as functions of (a) atomic ratios of Si to B for Ti-MWW-B materials, and (b) molar ratios of HF to TMAdaOH for Ti-MWW-F. ϕ_{IR} values were calculated using infrared absorption spectra (101 kPa He, 573 K) and Eq. 2.

protocols, other structural characteristics of these materials may differ, such as the location of Ti atoms and the proximity of $(\text{SiOH})_x$ defects to active sites.

Comparisons between the changes in product formation rates in response to *in situ* titration of active sites by diamines with distinct kinetic diameters provide evidence for the location of the Ti atoms that form active sites within the framework of Ti-MWW materials from different synthesis protocols. For example, smaller ED and bulkier DPED should titrate different populations of Ti atoms in MWW: ED may access all framework positions, including those in 10-membered sinusoidal channels and 12-membered supercages and side pockets. However, due to its steric bulk, DPED cannot enter the sinusoidal channels. Fig. 4 shows rates for C_6H_{12} epoxidation normalized by the rates without any titrants decrease monotonically the molar ratio of diamine titrants (ED or DPED) to Ti atoms (2 mM C_6H_{12} , 10 mM H_2O_2 , 39 mM H_2O , 313 K), and that the maximum extent of rate inhibition differs between these

titrants, as expected. Titrations performed with ED demonstrate that titrants can access all active sites within Ti-MWW. Importantly, epoxidation rates are undetectable when ED to Ti ratios are two and greater. Linear extrapolation of the ED titration curve at low ED to Ti ratios to the abscissa yields an intercept near unity, which suggests that nearly all Ti atoms within the samples form active sites [53]. In contrast, changes in rates following the addition of increasing molar ratios of DPED to Ti below 0.5 decrease product formation rates, however, the addition of greater quantities of DPED (DPED:Ti over 0.5) does not lead to further changes in rates. Upon reaching DPED to Ti ratios equal to two, epoxidation rates approach values equal to 30–35% of the rates measured in the absence of titrants. These non-zero residual rates with DPED, in combination with the complete suppression of reactivity with ED, demonstrate that DPED cannot access all Ti active sites in the MWW framework. The comparisons between these *in situ* titration curves (Fig. 4) give strong evidence that all Ti sites are catalytically active for C_6H_{12} epoxidation, ED titrates all active sites, and DPED selectively titrates active sites located in 12-membered supercages and side pockets but not the 10-membered sinusoidal channels of smaller dimensions (0.4–0.55 nm). Therefore, these titration methods and uptakes of DPED provide a method to quantify the populations of active sites (i.e., framework Ti atoms) present in each of these distinct environments.

With the knowledge that DPED binds exclusively to Ti atoms present in supercages and side pockets, measurements of DPED uptakes provide a quantitative measure of the number of Ti atoms in these locations. Consequently, the remaining Ti atoms (determined by EDXRF and titrations with ED) must reside in the more constrained 10-membered sinusoidal channels. The number of DPED molecules adsorbed to each Ti-MWW catalyst was measured under similar conditions for epoxidation without reactants present (CH_3CN solvent, 313 K) (Section 2.2). Comparisons between the adsorbed number of DPED molecules and the total number of Ti active sites give estimates for the fraction of Ti active sites that exist within 10-membered sinusoidal channels (χ_{sinusoid}) the values of which are given by Eq. 3

$$\chi_{\text{sinusoid}} = 1 - \frac{n_{\text{DPED}}}{n_{\text{Ti}}} \quad (3)$$

where n_{DPED} represents the number of adsorbed DPED molecules (determined by GC-FID from DPED uptake measurement, Section 2.2) and n_{Ti} is the number of Ti active sites (determined by EDXRF), both of which were measured for each Ti-MWW-B and Ti-MWW-F material.

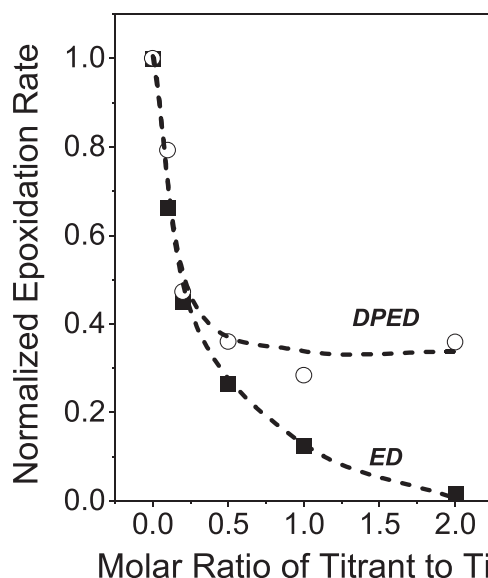


Fig. 4. Normalized rates for C_6H_{12} epoxidation as functions of the molar ratio of ED (■) or DPED (○) to framework Ti atoms for Ti-MWW-B(0.75) at standard conditions (2 mM C_6H_{12} , 10 mM H_2O_2 , 39 mM H_2O , 313 K).

Fig. 5 shows values of χ_{sinusoid} for Ti-MWW-B and Ti-MWW-F catalysts increase as linear functions of the Ti content (measured by EDXRF) of the oxidatively treated Ti-MWW catalysts. The trends in χ_{sinusoid} values across these materials give evidence that these synthesis protocols preferentially locate Ti atoms in supercages and side pockets of Ti-MWW catalysts at the lowest Ti contents, but greater fractions of Ti atoms occupy framework sites in confined sinusoidal channels as the Ti content increases. This result agrees with previous observations that showed decreased yields of bulky reactant (2-methyl-2-pentene) epoxidation with post-synthetically modified Ti-MWW zeolites with high Ti contents, which indirectly suggested the preferential location of Ti atoms in confined sinusoidal channels at greater Ti content [57]. While the span of values for χ_{sinusoid} and the range of Ti contents differ between Ti-MWW-B and Ti-MWW-F, values for χ_{sinusoid} obtained from both materials fall along a single linear correlation and suggest these methods do not differ in their preference to place Ti atoms at certain topological locations. Finally, values of χ_{sinusoid} across these materials do not correlate systematically with values of ϕ_{IR} , which demonstrates that the location of Ti atoms and the densities of $(\text{SiOH})_x$ depend upon independently controlled aspects of the synthesis protocol (e.g., atomic ratios of Si:Ti or Si:B). Consequently, these hydrothermal synthesis methods offer the means to change each of these characteristics of the Ti-MWW catalyst separately.

3.2. Epoxidation rates and reaction mechanism for Ti-MWW

Molecular insight into the reasons why epoxidation rates may depend upon the location of Ti atoms within the MWW structure and the influence of $(\text{SiOH})_x$ densities requires knowledge of the reaction mechanism and clear interpretations of parameters that determine turnover rates. **Fig. 6a** shows that turnover rates for the epoxidation of C_6H_{12} with H_2O_2 possess a strong dependence upon the concentration of C_6H_{12} ($[\text{C}_6\text{H}_{12}]$) (10 mM H_2O_2 , 313 K), and **Fig. 6b** demonstrates that rates depend differently on $[\text{H}_2\text{O}_2]$ at low (0.5 mM C_6H_{12}) and high (1 M C_6H_{12}) values of $[\text{C}_6\text{H}_{12}]$. These trends hold for all Ti-MWW-B and Ti-MWW-F catalysts ($[\text{C}_6\text{H}_{12}]$ dependencies for the other Ti-MWW catalysts are shown in **Fig. S5**), even though turnover rates (calculated from the total number of Ti atoms) vary by an order of magnitude at any given combination of reactant concentrations. When ratios of $[\text{H}_2\text{O}_2]$ to

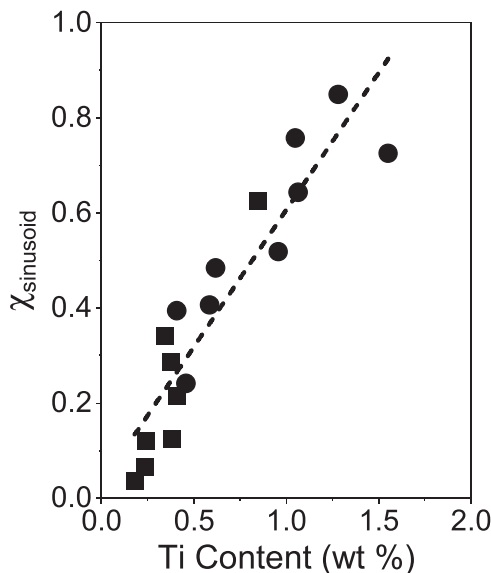


Fig. 5. Relative fractions of Ti sites in sinusoidal channels (χ_{sinusoid}) as a function of Ti weight loading (wt%) over Ti-MWW-B (■) and Ti-MWW-F (●). χ_{sinusoid} values were calculated via DPED uptake measurements (313 K) and Eq. 3.

$[\text{C}_6\text{H}_{12}]$ exceed a value of 10, epoxidation turnover rates increase linearly with $[\text{C}_6\text{H}_{12}]$ and subsequently reach a sublinear dependence on $[\text{C}_6\text{H}_{12}]$ when values of the ratio of $[\text{H}_2\text{O}_2]$ to $[\text{C}_6\text{H}_{12}]$ fall below two (10 mM H_2O_2 , 313 K). **Fig. 6b** shows that rates do not depend on $[\text{H}_2\text{O}_2]$ at the greatest $[\text{H}_2\text{O}_2]$ to $[\text{C}_6\text{H}_{12}]$ ratios (0.1 mM C_6H_{12} , 313 K) but exhibit a near first-order dependence on $[\text{H}_2\text{O}_2]$ when $[\text{C}_6\text{H}_{12}]$ surpasses $[\text{H}_2\text{O}_2]$ by a factor of at least 10 (1 M C_6H_{12} , 313 K). In addition, **Fig. 7** demonstrates that rates decrease with the concentration of 1,2-epoxyhexane ($[\text{C}_6\text{H}_{12}\text{O}]$) at $[\text{C}_6\text{H}_{12}]$ to $[\text{H}_2\text{O}_2]$ ratio of 50. These apparent rate dependencies appear for all Ti-MWW catalysts, regardless of the composition or the synthesis method.

Scheme 1 presents a sequence of elementary steps that account for these observations on Ti-MWW and that agree with proposed mechanisms for epoxidations of alkenes with H_2O_2 on other metal-incorporated zeotype catalysts [16–20,45,53,58]. The C_6H_{12} reagent adsorbs to the Ti center in a quasi-equilibrated manner (step 1), as does H_2O_2 (step 2). Subsequently, Ti sites activate adsorbed H_2O_2 species irreversibly to form a pool of reactive intermediates that includes Ti-hydroperoxide (Ti-OOH) and Ti-peroxo ($\text{Ti}-\eta^2-\text{O}_2$) species, observed in previous studies via *in situ* Raman and UV-Vis spectroscopic analyses in the liquid-phase system [53]. Also, cis-stilbene epoxidation kinetics revealed that Ti-OOH intermediates mainly drive the oxygen atom transfer step to C_6H_{12} reagent during epoxidation; therefore, in this study, we define Ti-OOH as the activated H_2O_2 intermediates in the following context. The Ti-OOH species either transfer O-atoms to epoxidize C_6H_{12} and produce H_2O in a kinetically relevant step (step 4) or decompose to produce O_2 and H_2O through reaction with another H_2O_2 molecule (step 6). The 1,2-epoxyhexane ($[\text{C}_6\text{H}_{12}\text{O}]$) desorbs from Ti centers in a quasi-equilibrated fashion (step 5) to regenerate the active site. Applying the law of mass action to the elementary steps and invoking the pseudo-steady state hypothesis upon the number of Ti-OOH intermediates ($[\text{Ti-OOH}]$) leads to an analytical expression for the turnover rate for C_6H_{12} epoxidation (Eq. 4)

$$\frac{r_E}{[\text{L}]} = \frac{\frac{k_3 k_4 K_2 [\text{H}_2\text{O}_2] [\text{C}_6\text{H}_{12}]}{k_4 [\text{C}_6\text{H}_{12}] + k_6 [\text{H}_2\text{O}_2]}}{1 + K_1 [\text{C}_6\text{H}_{12}] + K_2 [\text{H}_2\text{O}_2] + \frac{k_3 K_2 [\text{H}_2\text{O}_2]}{k_4 [\text{C}_6\text{H}_{12}] + k_6 [\text{H}_2\text{O}_2]} + \frac{[\text{C}_6\text{H}_{12}\text{O}]}{K_5}}} \quad (4)$$

where the turnover rate of C_6H_{12} epoxidation is represented as $r_E/[\text{L}]$, rate constants for each step i as k_i , and equilibrium constants for quasi-equilibrated steps as K_i . A complete derivation for this rate expression appears in the **Supporting Information** (Section S2.2). When the H_2O_2 -derived species (Ti-OOH) as the most abundant reactive intermediates (MARI) on Ti sites leads to the cancellation of multiple terms in the denominator and numerator of Eq. 4, which leads to a simpler form [53, 59]

$$\frac{r_E}{[\text{L}]} = k_4 [\text{C}_6\text{H}_{12}] \quad (5)$$

This result corresponds to the observed first-order $[\text{C}_6\text{H}_{12}]$ and zero-order $[\text{H}_2\text{O}_2]$ dependence of the epoxidation turnover rate at a low $[\text{C}_6\text{H}_{12}]$ to $[\text{H}_2\text{O}_2]$ ratio < 0.1 . Increasing $[\text{C}_6\text{H}_{12}]$ leads to the shifts in MARI from the activated H_2O_2 species to the surface-adsorbed C_6H_{12} and $\text{C}_6\text{H}_{12}\text{O}$ species. In these MARI regimes, turnover rates could show an increasing trend with $[\text{H}_2\text{O}_2]$ (**Fig. 6b**, gray data with 1 M C_6H_{12} and 10 mM H_2O_2) which corresponds to Eq. 4 with high $[\text{C}_6\text{H}_{12}]$,

$$\frac{r_E}{[\text{L}]} = \frac{k_3 k_4 K_2 [\text{H}_2\text{O}_2]}{K_1 (k_4 [\text{C}_6\text{H}_{12}] + k_6 [\text{H}_2\text{O}_2])} \quad (6)$$

or a decreasing trend with $[\text{C}_6\text{H}_{12}\text{O}]$ (**Fig. 7**).

$$\frac{r_E}{[\text{L}]} = \frac{k_3 k_4 K_2 K_5 [\text{H}_2\text{O}_2] [\text{C}_6\text{H}_{12}]}{(k_4 [\text{C}_6\text{H}_{12}] + k_6 [\text{H}_2\text{O}_2]) [\text{C}_6\text{H}_{12}\text{O}]} \quad (7)$$

Collectively, the measured rates match with the proposed C_6H_{12} epoxidation mechanism, and the choice of SDA and its composition do not affect the reaction mechanism since the trends of the epoxidation

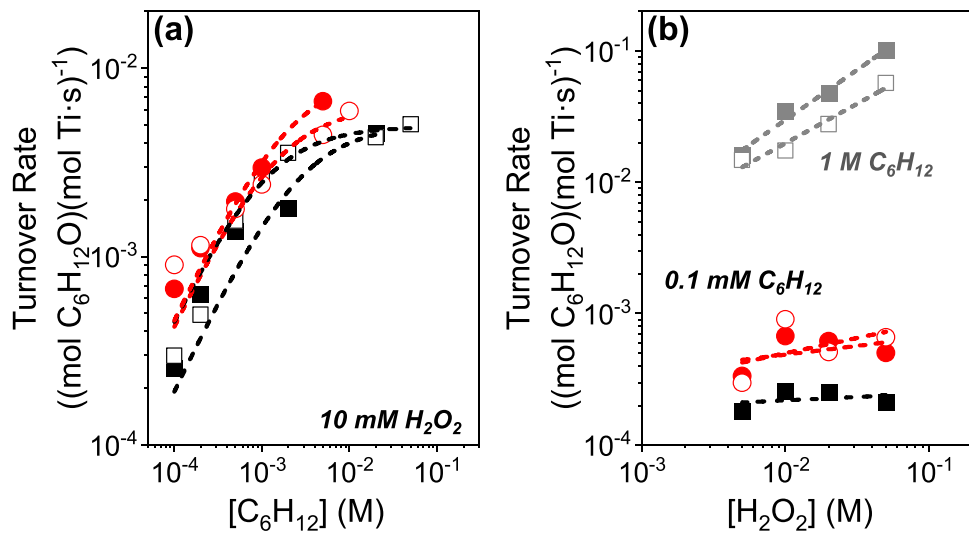


Fig. 6. Turnover rates for C₆H₁₂ epoxidation with H₂O₂ as a function of (a) [C₆H₁₂] (10 mM H₂O₂, 39 mM H₂O, 313 K), and (b) [H₂O₂] (0.1 mM C₆H₁₂ (black and red) or 1 M C₆H₁₂ (gray), 313 K) over Ti-MWW-B(0.5) (black and gray ■, Si:Ti = 100), Ti-MWW-B(1.5) (black and gray □, Si:Ti = 100), Ti-MWW-F(0) (red ●, Si:Ti = 50), and Ti-MWW-F(0.5) (red ○, Si:Ti = 50).

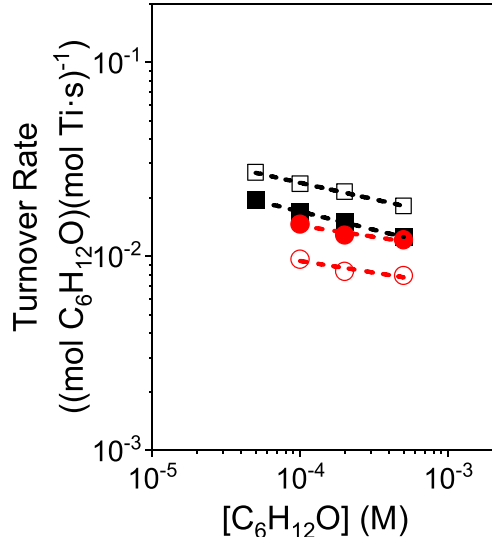
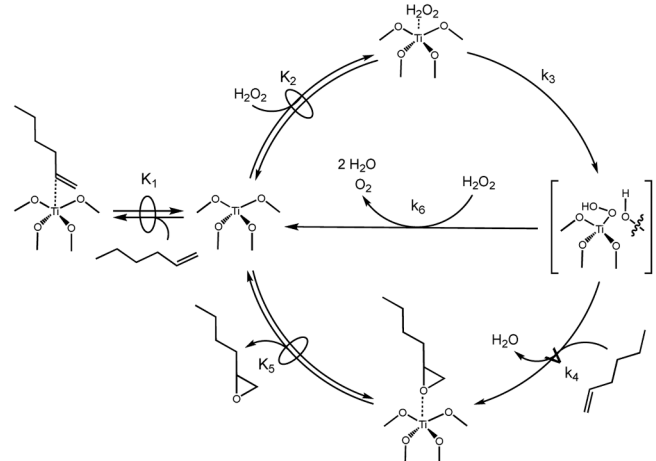


Fig. 7. Turnover rates for C₆H₁₂ epoxidation with H₂O₂ as a function of [C₆H₁₂O] over Ti-MWW-B(0.5) (black ■, Si:Ti = 100), Ti-MWW-B(1.5) (black □, Si:Ti = 100), Ti-MWW-F(0) (red ●, Si:Ti = 50), and Ti-MWW-F(0.5) (red ○, Si:Ti = 50) (500 mM C₆H₁₂, 10 mM H₂O₂, 39 mM H₂O, 313 K).

turnover rate at various reactant concentrations do not change across Ti-MWW catalysts.

3.3. Impact of interactions among reactive intermediates, solvent molecules, and confining voids on epoxidation kinetics

Differences in turnover rates for epoxidation between Ti-MWW materials reflect the values of their apparent rate constants (k_4 , when Ti-OOH saturates active sites), which depend upon standard free energy differences ($\Delta G^{\ddagger,0}$) that report on covalent and ionic interactions but also excess free energy changes ($\Delta G^{\ddagger,e}$) associated with noncovalent interactions (e.g., hydrogen bonds) that vary with the structure of reactive intermediates, topology and polarity of the surrounding void, and the organization of solvent molecules [15–17]. Prior work demonstrates that solvent molecules (e.g., CH₃CN [16,18,19,43], H₂O [45], CH₃OH [20,43], etc.) reorganize to accommodate adsorption of bulky



Scheme 1. Proposed mechanism of C₆H₁₂ epoxidation with the presence of H₂O₂ over Ti-MWW catalysts. \xrightarrow{A} symbol emphasizes the kinetically relevant step for the epoxidation, and quasi-equilibrated elementary steps are denoted with \xrightleftharpoons{E} symbol.

molecules to active sites and the formation of transition states for alkene epoxidation at these same active sites: both processes lead to excess enthalpy (H^\ddagger) and entropy (S^\ddagger) contributions that cause turnover rates to vary over orders of magnitude [16,17]. These physical processes also lead to large differences in apparent activation barriers (ΔH^\ddagger , ΔS^\ddagger) for epoxidations within Ti-MWW catalysts, which may be controlled via synthesis protocols that influence the density of (SiOH)_x defects or the position of Ti atoms (i.e., in 10-membered ring sinusoidal channels or 12-membered ring supercages) within Ti-MWW catalysts.

Fig. 8a shows epoxidation turnover rates as a function of ϕ_{IR} values at conditions of Ti-OOH intermediates dominating surfaces (0.5 mM C₆H₁₂, 10 mM H₂O₂, 39 mM H₂O, 313 K). Overall, the rates across Ti-MWW catalysts do not show systematic changes with ϕ_{IR} values, and several extreme outliers suggest that values of ϕ_{IR} do not provide a complete descriptor for reactivity, which contradicts findings from other Ti-zeolite catalysts, showing 10 (Ti-FAU) [17], 80 (Ti-MFI) [20], and 100 (Ti-BEA)-fold [17,18] increases in C₆H₁₂ epoxidation turnover rates in CH₃CN. Notably, the catalysts compared in Fig. 8 include two different synthesis methods and a range of Si to Ti ratios (50–200).

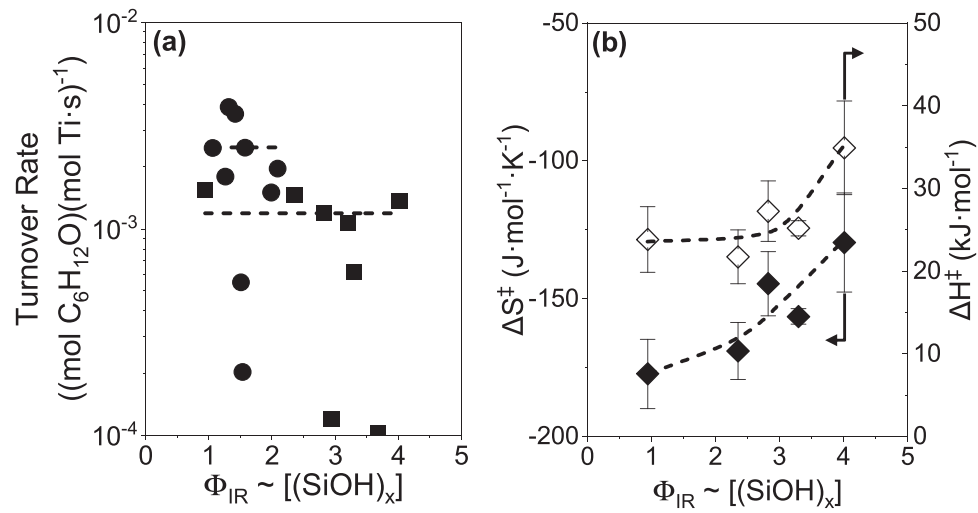


Fig. 8. (a) Turnover rates for C₆H₁₂ epoxidation with H₂O₂ over Ti-MWW-B (■) and Ti-MWW-F (●) (0.5 mM C₆H₁₂, 10 mM H₂O₂, 39 mM H₂O, 313 K), and (b) apparent activation entropies (ΔS^\ddagger , ◆) and enthalpies (ΔH^\ddagger , ◇) for C₆H₁₂ epoxidation with H₂O₂ over Ti-MWW-B (Si:Ti = 100) as functions of relative (SiOH)_x densities (ϕ_{IR}) (0.1 mM C₆H₁₂, 10 mM H₂O₂, 39 mM H₂O, 303–328 K). ϕ_{IR} values were calculated using infrared absorption spectra (101 kPa He, 573 K) and Eq. 2.

Comparisons of activation barriers among Ti-MWW catalysts with similar Si to Ti ratios and formed by identical protocols give evidence that variations in (SiOH)_x do introduce excess contributions that impact epoxidation kinetics. Fig. 8b shows the apparent activation entropies (ΔS^\ddagger) and enthalpies (ΔH^\ddagger) for the C₆H₁₂ epoxidation reaction as functions of ϕ_{IR} over Ti-MWW-B catalysts with Si:Ti ratio of 100 (0.1 mM C₆H₁₂, 10 mM H₂O₂, 39 mM H₂O, 303–333 K), which are calculated from turnover rates measured as functions of inverse temperature (Supporting Information Section S2.3) as described in Eq. 8.

$$\frac{r_E}{[L]} = \frac{k_B T}{h} e^{-\frac{\Delta H^\ddagger}{RT}} e^{\frac{\Delta S^\ddagger}{R}} [C_6H_{12}] \quad (8)$$

where k_B and h are Boltzmann and Planck constants, R depicts the ideal gas constant, and T is the absolute temperature (K) at which the reaction occurs. By comparing these Ti-MWW-B catalysts (Si:Ti = 100), we are able to minimize the potential effects of relative Ti site locations on rates since these samples show the slightest differences in the active site distributions (predominantly located in 12-membered supercages, $0.07 \leq \chi_{\text{sinusoid}} \leq 0.34$) while exhibiting drastic (SiOH)_x density differences (i.e., 4-fold increase).

Fig. 8b shows values of ΔS^\ddagger and ΔH^\ddagger for C₆H₁₂ epoxidation increase systematically with ϕ_{IR} values from -177 to -129 J·mol⁻¹·K⁻¹ (by 48 J·mol⁻¹·K⁻¹) and from 24 to 35 kJ·mol⁻¹ (by 11 kJ·mol⁻¹), respectively. Previous report of Ti-BEA with more confined voids (0.65 nm pores) shows ΔS^\ddagger and ΔH^\ddagger differences between hydrophilic and hydrophobic materials by 105 J·mol⁻¹·K⁻¹ and 16 kJ·mol⁻¹, respectively, in similar reaction conditions (0.5 mM C₆H₁₂, 10 mM H₂O₂, 39 mM H₂O, 313 K), which signify greater average disruption of intrapore solvent networks inside the slightly smaller pores of *BEA [17]. Ti-MFI materials, on the other hand, exhibit a lesser increase in ΔH^\ddagger (4 kJ·mol⁻¹) but a comparable increase in ΔS^\ddagger (53 J·mol⁻¹·K⁻¹) in hydrophilic pores, in part, because the excess contributions influence the stability of Ti-OOH intermediates to a greater extent in the more confined pore environments. Collectively, the magnitude of the increases in ΔS^\ddagger and ΔH^\ddagger across Ti-MWW catalysts due to the unique structures lead to similar epoxidation turnover rates and activation free energies for C₆H₁₂ epoxidation (Fig. 8a).

Differences in reaction rates across Ti-incorporated MWW catalysts also reflect the topological locations of catalytic active sites within the MWW zeolite framework [14,29,32]. Fig. 9 shows turnover rates for C₆H₁₂ epoxidation over Ti-MWW-B and Ti-MWW-F increase by 40-fold as the fraction of Ti atoms in 10-membered sinusoidal channels

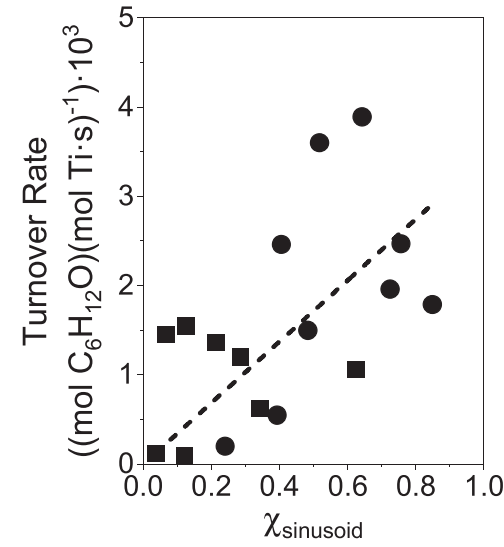


Fig. 9. Turnover rates for C₆H₁₂ epoxidation with H₂O₂ over Ti-MWW-B (■) and Ti-MWW-F (●) as a function of relative fractions of Ti sites in sinusoidal channels (χ_{sinusoid}) (0.5 mM C₆H₁₂, 10 mM H₂O₂, 39 mM H₂O, 313 K). χ_{sinusoid} values were calculated via DPED uptake measurements (313 K) and Eq. 3.

increases ($0.1 \leq \chi_{\text{sinusoid}} \leq 0.8$) at conditions where Ti-OOH intermediates dominate Ti active sites (0.5 mM C₆H₁₂, 10 mM H₂O₂, 39 mM H₂O, 313 K). This trend seems consistent with prior work that demonstrated a 60% increase in turnover number for C₆H₁₂ epoxidation increasing Ti content of the Ti-MWW materials ($50 < \text{Si:Ti} < 20$) [29], which we expect resulted in greater fractions of Ti atoms in sinusoidal channels.

These significant increases in apparent turnover rates (normalized by the total number of Ti atoms) appear to result from the greater fractions of Ti sites that reside in sinusoidal channels. The smaller dimensions of these channels seem likely to confer S^e and H^e values distinct from those in supercages, because the magnitude of excess contributions depends strongly on the pore topology of zeolites [17,42]. Fig. 10 compares values of ΔS^\ddagger and ΔH^\ddagger measured on Ti-MWW-B(0.75) in the absence and presence of DPED (DPED:Ti = 1.4). The addition of DPED inhibits catalysis at Ti sites located within 12-membered supercages and side pockets (vide supra, Section 3.1). Consequently, ΔS^\ddagger and ΔH^\ddagger values

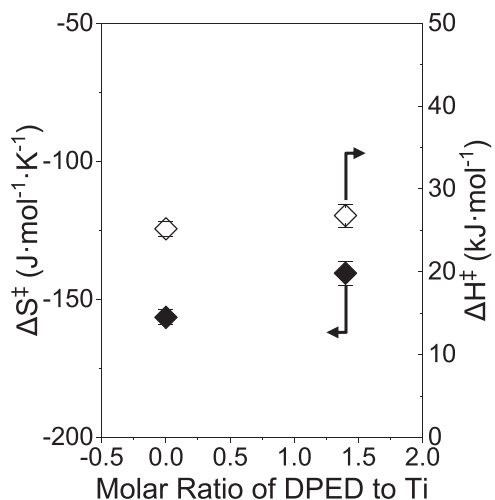


Fig. 10. Apparent activation entropies (ΔS^\ddagger ; ◆) and enthalpies (ΔH^\ddagger ; ◇) for C_6H_{12} epoxidation with H_2O_2 as a function of the molar ratio of DPED to framework Ti atoms for Ti-MWW-B(0.75) (0.1 mM C_6H_{12} , 10 mM H_2O_2 , 39 mM H_2O , 303–328 K).

measured with DPED represent the kinetics of reaction events at active sites within 10-membered ring sinusoidal channels, whereas values in the absence of DPED provide a Boltzmann average across Ti sites in all regions of the pore structure.

The addition of DPED (DPED:Ti = 1.4) leads to ΔS^\ddagger values that are more positive by $16\text{ J}\cdot\text{mol}^{-1}\cdot\text{K}^{-1}$ (by taking epoxidation rates normalized by the number of available Ti sites after DPED poisoning) in comparison to values measured without DPED, while values of ΔH^\ddagger remain nearly constant (increase by $1.6\text{ kJ}\cdot\text{mol}^{-1}$, within uncertainty range). These comparisons suggest that the formation of epoxidation transition states yields more significant entropic benefits in confined sinusoidal channels (i.e., measurements with DPED) than in open supercages and side pockets (i.e., measurements without DPED). This agrees with the prior results showing more significant disruption of hydrogen-bonded solvent networks in small-dimension zeolite framework (e.g., Ti-MFI and Ti-BEA) than larger pore materials (e.g., Ti-FAU) [16,17]. The increase in ΔS^\ddagger surpasses the slightly increased ΔH^\ddagger penalty at the Ti sites in the sinusoidal channels, leading to the lower overall activation energy of the C_6H_{12} epoxidation and higher rates. This result also corroborates the lesser entropic benefits in Ti-MWW catalysts than the other Ti-zeolite catalysts (e.g., Ti-BEA) during the formation of C_6H_{12} epoxidation transition states (Section 3.3). Since most Ti active sites in Ti-MWW-B catalysts with varying $(SiOH)_x$ densities are located in the large supercages ($1.82 \times 0.71\text{ nm}$) and side pockets ($Si:Ti = 100$, $\chi_{\text{sinusoid}} \leq 0.34$), active sites in Ti-BEA pores ($0.65 \times 0.65\text{ nm}$) [60,61] could yield more positive energetic effects in hydrophilic pores on rates than Ti-MWW, possibly with reorganized intrapore solvent structures, resulting in more significant differences in rates between hydrophilic and hydrophobic pores. Consequently, the energetic effects during transition state formation influence C_6H_{12} epoxidation rates differently (by 40-fold), depending on the topological locations of Ti active sites in the MWW framework.

4. Conclusion

Pore microenvironments in the vicinity of active sites significantly affect the alkene epoxidation with H_2O_2 over MWW-type zeolite catalysts. Topological locations of Ti active sites in MWW pore structures and relative density of $(SiOH)_x$ defects near active sites can be tuned by varying the species and quantity of structure-directing agents during the hydrothermal synthesis. We synthesized Ti-MWW catalysts by introducing two hydrothermal synthesis methods and adding different

amounts of H_3BO_3 and HF for Ti-MWW-B and Ti-MWW-F, respectively, in order to control the relative $(SiOH)_x$ densities. Relative $(SiOH)_x$ densities decrease by the factors of 4 and 2 in Ti-MWW-B and Ti-MWW-F catalysts, by increasing the atomic ratios of Si:B and the molar ratios of HF:TMAdaOH, respectively. Ti active sites are incorporated within various MWW pores (i.e., 12-membered supercages, side pockets, and 10-membered sinusoidal channels), and the relative locations of Ti sites were varied by changing the quantity of Ti atoms. Uptake measurements with the bulky titrant DPED suggest that most Ti atoms are located within more open 12-membered supercages and side pockets at low Ti loading. Ti atoms become more evenly distributed between open 12-membered sites and confined 10-membered sinusoidal channels with increased loadings. Collectively, varying the conditions during the hydrothermal synthesis of Ti-MWW catalysts leads to measurable differences in the physical properties of MWW pores and Ti active sites.

Liquid-phase batch reactions of C_6H_{12} epoxidation signify effects of Ti site locations and relative $(SiOH)_x$ densities on the epoxidation mechanism and excess energetic effects on turnover rates. At high $[H_2O_2]$ to $[C_6H_{12}]$ ratios over 10, C_6H_{12} epoxidation rates follow a first-order dependence of $[C_6H_{12}]$ and a weak dependence on $[H_2O_2]$, revealing that H_2O_2 -derived intermediate (Ti-OOH) exists as dominating surface intermediates. In lower $[H_2O_2]$ to $[C_6H_{12}]$ ratios below 10, alkene reactant and epoxide product (C_6H_{12} , $C_6H_{12}O$) dominate metal surface and show increasing rate dependencies on $[H_2O_2]$ and decreasing dependencies on $[C_6H_{12}O]$. Under the Ti-OOH-dominated regime, turnover rates of C_6H_{12} remain relatively constant over Ti-MWW with varying $(SiOH)_x$ densities. Apparent activation enthalpies and entropies for C_6H_{12} epoxidation suggest that the formation of transition states possibly disrupts hydrogen-bonded solvent networks (CH_3CN and H_2O) inside the confined MWW structures. Thus, the transition state of the epoxidation becomes entropically more stable by $48\text{ J}\cdot\text{mol}^{-1}\cdot\text{K}^{-1}$ with a higher density of $(SiOH)_x$, but this entropic gain does not fully compensate for the enthalpic penalties ($11\text{ kJ}\cdot\text{mol}^{-1}$), resulting in unchanging rates with $(SiOH)_x$ densities. C_6H_{12} epoxidation rates increase up to 40 times at Ti sites located in more confined 10-membered sinusoidal channels relative to the Ti sites in more open 12-membered supercages and side pockets. Due to the confinement of smaller pore structures near the Ti sites, the entropic benefit of the transition states (increase by $16\text{ J}\cdot\text{mol}^{-1}\cdot\text{K}^{-1}$) in sinusoidal channels leads to the lower apparent activation free energy of the transition state and higher rates than in the supercages and side pockets.

These findings suggest that epoxidation kinetics respond to the controlled physical properties of metal-zeolite pore structures, which provide insights into designing a catalytic system involving microporous zeolite catalysts in the presence of organic solvents condensed inside pores. These findings of fine-tuning active site locations and defect densities over zeolite-based catalysis could extend to various chemical and industrial applications.

CRediT authorship contribution statement

Ohsung Kwon: Writing – review & editing, Writing – original draft, Visualization, Validation, Software, Resources, Methodology, Investigation, Formal analysis, Data curation, Conceptualization. **David S. Potts:** Writing – review & editing, Methodology, Investigation, Data curation, Conceptualization. **David W. Flaherty:** Writing – review & editing, Validation, Supervision, Project administration, Methodology, Investigation, Funding acquisition, Data curation.

Declaration of Competing Interest

The authors declare that they have no known competing financial interests or personal relationships that could have appeared to influence the work reported in this paper.

Data availability

Data will be made available on request.

Acknowledgements

XRD, EDXRF, and DRUV-Vis measurements were conducted in the Frederic Seitz Materials Research Laboratory, and ICP-OES analysis was performed in the Microanalysis Laboratory of the School of Chemical Sciences at the University of Illinois Urbana-Champaign. This material is based upon work supported by the U.S. Department of Energy, Office of Science, Office of Basic Energy Sciences (award number DE-SC0020224). OK acknowledges the Samuel W. Parr Fellowship from the University of Illinois Urbana-Champaign.

Appendix A. Supporting information

Supplementary data associated with this article can be found in the online version at [doi:10.1016/j.apcatb.2024.124119](https://doi.org/10.1016/j.apcatb.2024.124119).

References

- [1] M. Prasad, S. Caspa, R.V.D.L. Sandra, P. Ron, 2017, (<https://doi.org/084-355-184-639-052>), Process For The Manufacture Of Propylene Oxide.
- [2] V. Russo, R. Tesser, E. Santacesaria, M. Di Serio, Chemical and technical aspects of propene oxide production via hydrogen peroxide (HPPO process), Ind. Eng. Chem. Res. 52 (2013) 1168–1178, <https://doi.org/10.1021/ie3023862>.
- [3] F. Schmidt, M. Bernhard, H. Morell, M. Pascaly, HPPO process technology A novel route to propylene oxide without coproducts, Chim. Oggi/Chem. Today 32 (2014) 31–35.
- [4] P. Bassler, H.G. Göbbel, M. WeidenbachThe new HPPO process for propylene oxide: From joint development to worldscale production Italian Association of Chemical Engineering - AIDIC , Chem. Eng. Trans. , 2010, 571–576, 10.3303/CET1021096.
- [5] L. Wu, S. Zhao, L. Lin, X. Fang, Y. Liu, M. He, In-depth understanding of acid catalysis of solvolysis of propene oxide over titanosilicates and titanosilicate/H2O2 systems, J. Catal. 337 (2016) 248–259, <https://doi.org/10.1016/j.jcat.2016.01.028>.
- [6] M. Lin, C. Xia, B. Zhu, H. Li, X. Shu, Green and efficient epoxidation of propylene with hydrogen peroxide (HPPO process) catalyzed by hollow TS-1 zeolite: a 1.0 kt/a pilot-scale study, Chem. Eng. J. 295 (2016) 370–375, <https://doi.org/10.1016/j.cej.2016.02.072>.
- [7] G. Prieto, F. Schüth, The Yin and Yang in the development of catalytic processes: catalysis research and reaction engineering, Angew. Chem. Int. Ed. 54 (2015) 3222–3239, <https://doi.org/10.1002/anie.201409885>.
- [8] A. Thangaraj, S. Sivasanker, P. Ratnasamy, Catalytic properties of crystalline titanium silicalites III. Ammonoxidation of cyclohexanone, J. Catal. 131 (1991) 394–400, [https://doi.org/10.1016/0021-9517\(91\)90274-8](https://doi.org/10.1016/0021-9517(91)90274-8).
- [9] M.G. Clerici, G. Bellussi, U. Romano, Synthesis of propylene oxide from propylene and hydrogen peroxide catalyzed by titanium silicalite, J. Catal. 129 (1991) 159–167, [https://doi.org/10.1016/0021-9517\(91\)90019-Z](https://doi.org/10.1016/0021-9517(91)90019-Z).
- [10] P. Andrei-Nicolae, M. Ulrich, T.J. Henrique, S. Bianca, K. Philip, W. Markus, B. Robert, S. Karsten, R. Peter, 2013, (<https://doi.org/007-865-291-704-435>) , Micropowder And Molding Containing A Zeolitic Material Containing Ti And Zn.
- [11] G. Wang, Y. Li, Q. Zhu, G. Li, C. Zhang, H. Guo, Influence of impurities in a methanol solvent on the epoxidation of propylene with hydrogen peroxide over titanium silicalite-1, Catalysts 10 (2020), <https://doi.org/10.3390/catal10010015>.
- [12] F. Song, Y. Liu, L. Wang, H. Zhang, M. He, P. Wu, Highly Efficient Epoxidation of Propylene over A Novel Ti-MWW Catalyst. Stud. Surf. Sci. Catal., Elsevier Inc, 2007, pp. 1236–1243, [https://doi.org/10.1016/S0167-2991\(07\)80983-9](https://doi.org/10.1016/S0167-2991(07)80983-9).
- [13] X. Lu, H. Wu, J. Jiang, M. He, P. Wu, Selective synthesis of propylene oxide through liquid-phase epoxidation of propylene with H2O2 over formed Ti-MWW catalyst, J. Catal. 342 (2016) 173–183, <https://doi.org/10.1016/j.jcat.2016.07.020>.
- [14] P. Wu, T. Tatsumi, A novel titanasilicate with MWW structure III. Highly efficient and selective production of glycidol through epoxidation of allyl alcohol with H2O2, J. Catal. 214 (2003) 317–326, [https://doi.org/10.1016/S0021-9517\(02\)00170-7](https://doi.org/10.1016/S0021-9517(02)00170-7).
- [15] D.S. Potts, D.T. Bregante, J.S. Adams, C. Torres, D.W. Flaherty, Influence of solvent structure and hydrogen bonding on catalysis at solid-liquid interfaces, Chem. Soc. Rev. 50 (2021) 12308–12337, <https://doi.org/10.1039/DICS00539A>.
- [16] D.T. Bregante, A.M. Johnson, A.Y. Patel, E.Z. Ayla, M.J. Cordon, B.C. Bukowski, J. Greeley, R. Gounder, D.W. Flaherty, Cooperative effects between hydrophilic pores and solvents: catalytic consequences of hydrogen bonding on alkene epoxidation in zeolites, J. Am. Chem. Soc. 141 (2019) 7302–7319, <https://doi.org/10.1021/jacs.8b12861>.
- [17] D.T. Bregante, M.C. Chan, J.Z. Tan, E.Z. Ayla, C.P. Nicholas, D. Shukla, D. W. Flaherty, The shape of water in zeolites and its impact on epoxidation catalysis, Nat. Catal. 4 (2021) 797–808, <https://doi.org/10.1038/s41929-021-00672-4>.
- [18] D.S. Potts, V.S. Jeyaraj, O. Kwon, R. Ghosh, A.V. Mironenko, D.W. Flaherty, Effect of Interactions between alkyl chains and solvent structures on Lewis Acid catalyzed epoxidations, ACS Catal. 12 (2022) 13372–13393, https://doi.org/10.1021/ACSCATAL_2C03493.
- [19] O. Kwon, E.Z. Ayla, D.S. Potts, D.W. Flaherty, Effects of solvent-pore interaction on rates and barriers for vapor phase alkene epoxidation with gaseous H2O2 in Ti-BEA catalysts, ACS Catal. 13 (2023) 6430–6444, https://doi.org/10.1021/ACSCATAL_3C00730.
- [20] C. Torres, D.S. Potts, D.W. Flaherty, Solvent mediated interactions on alkene epoxidations in Ti-MFI: effects of solvent identity and silanol density, ACS Catal. (2023) 8925–8942, https://doi.org/10.1021/ACSCATAL_3C01073/ASSET_IMAGES/LARGE/CS3C01073_0008.JPG.
- [21] M. Cordon, J.W. Harris, J.C. Vega-Vila, J.S. Bates, S. Kaur, M. Gupta, M.E. Witzke, E.C. Wegener, J.T. Miller, D.W. Flaherty, D.D. Hibbitts, R. Gounder, Dominant role of entropy in stabilizing sugar isomerization transition states within hydrophobic zeolite pores, J. Am. Chem. Soc. 140 (2018) 14244–14266, <https://doi.org/10.1021/jacs.8b08336>.
- [22] J.R. Di Iorio, B.A. Johnson, Y. Román-Leshkov, Ordered hydrogen-bonded alcohol networks confined in lewis acid zeolites accelerate transfer hydrogenation turnover rates, J. Am. Chem. Soc. 142 (2020) 19379–19392, https://doi.org/10.1021/JACS.0C09825/SUPPL_FILE/JAOC09825_SI_001.PDF.
- [23] X. Fan, W. Hu, S. Jin, G. Tao, Z. Tang, C. Wang, H. Sun, W. Yang, Effect of P modification on the structure and catalytic performance of Ti-MWW zeolite, Microporous Mesoporous Mater. 336 (2022) 111887, <https://doi.org/10.1016/J.MICROMESO.2022.111887>.
- [24] J. Chu, Z. Ge, J. Peng, H. Hu, S. Guo, X. Chen, Synthesis of Ti-MWW zeolite by refluxing and implanting titanium method and further application in 1-hexene epoxidation, Catal. Lett. 1 (2022) 1–16, <https://doi.org/10.1007/S10562-022-03964-X/FIGURES/12>.
- [25] C.B. Dartt, M.E. Davis, Characterization and catalytic activity of titanium containing SSZ-33 and aluminum-free zeolite beta, Appl. Catal. A Gen. 143 (1996) 53–73, [https://doi.org/10.1016/0926-860X\(96\)00070-1](https://doi.org/10.1016/0926-860X(96)00070-1).
- [26] C.P. Gordon, H. Engler, A.S. Tragl, M. Plodinec, T. Lunkenbein, A. Berkessel, J. H. Teles, A.N. Parvulescu, C. Copéret, Efficient epoxidation over dinuclear sites in titanium silicalite-1, Nature 586 (2020) 708–713, <https://doi.org/10.1038/s41586-020-2826-3>.
- [27] A. Corma, P. Esteve, A. Martínez, Solvent effects during the oxidation of olefins and alcohols with hydrogen peroxide on Ti-beta catalyst: the influence of the hydrophilicity-hydrophobicity of the zeolite, J. Catal. 161 (1996) 11–19, <https://doi.org/10.1006/jcat.1996.0157>.
- [28] T. Long-Xiang, Z. Feng-Mei, L. Dong-Fan, Z. Lu-Bin, Characteristics of the poisoning effect of nickel deposited on USY zeolite, Appl. Catal. A, Gen. 91 (1992) 67–80, [https://doi.org/10.1016/0926-860X\(92\)85066-K](https://doi.org/10.1016/0926-860X(92)85066-K).
- [29] P. Wu, T. Tatsumi, T. Komatsu, T. Yashimay, A novel titanasilicate with MWW structure: II. Catalytic properties in the selective oxidation of alkenes, J. Catal. 202 (2001) 245–255, <https://doi.org/10.1006/jcat.2001.3278>.
- [30] C. Baerlocher, D.H. Olson, W.M. Meier, Atlas of Zeolite Framework Types (formerly: Atlas of Zeolite Structure Types), Elsevier Science, 2001. (<https://books.google.com/books?id=c5JGbc7VZgC>).
- [31] D. Zhou, H. Zhang, J. Zhang, X. Sun, H. Li, N. He, W. Zhang, Density functional theory investigations into the structure and spectroscopic properties of the Ti4+ species in Ti-MWW zeolite, Microporous Mesoporous Mater. 195 (2014) 216–226, <https://doi.org/10.1016/j.micromeso.2014.04.037>.
- [32] J. Yin, H. Xu, B. Wang, W. Tian, J. Yin, J. Jiang, P. Wu, Highly selective 1-pentene epoxidation over Ti-MWW with modified microenvironment of Ti active sites, Catal. Sci. Technol. 10 (2020) 6050–6064, <https://doi.org/10.1039/d0cy00478b>.
- [33] N.A. Grosso-Giordano, A.S. Hoffman, A. Boubnov, D.W. Small, S.R. Bare, S.I. Zones, A. Katz, Dynamic reorganization and confinement of TiIV active sites controls olefin epoxidation catalysis on two-dimensional zeotypes, J. Am. Chem. Soc. 141 (2019) 7090–7106, <https://doi.org/10.1021/jacs.9b02160>.
- [34] H. Zhao, T. Yokoi, J.N. Kondo, T. Tatsumi, Hydrophobicity enhancement of Ti-MWW catalyst and its improvement in oxidation activity, Appl. Catal. A Gen. 503 (2015) 156–164, <https://doi.org/10.1016/j.apcata.2015.07.003>.
- [35] L. Wang, Y. Liu, W. Xie, H. Wu, X. Li, M. He, P. Wu, Improving the hydrophobicity and oxidation activity of Ti-MWW by reversible structural rearrangement, J. Phys. Chem. C. 112 (2008) 6132–6138, <https://doi.org/10.1021/JP712155K/F0001.JPG>.
- [36] X. Fang, Q. Wang, A. Zheng, Y. Liu, L. Lin, H. Wu, F. Deng, M. He, P. Wu, Post-synthesis, characterization and catalytic properties of fluorine-planted MWW-type titanasilicate, Phys. Chem. Chem. Phys. 15 (2013) 4930–4938, <https://doi.org/10.1039/c3cp44700f>.
- [37] X. Fang, Q. Wang, A. Zheng, Y. Liu, Y. Wang, X. Deng, H. Wu, F. Deng, M. He, P. Wu, Fluorine-planted titanasilicate with enhanced catalytic activity in alkene epoxidation with hydrogen peroxide, Catal. Sci. Technol. 2 (2012) 2433–2435, <https://doi.org/10.1039/c2cy20446k>.
- [38] S. Guo, Y. Zhang, Y. Ye, J. Song, M. Li, MWW-Type titanasilicate synthesized by simply treating ERB-P zeolite with acidic H2TiF6 and its catalytic performance in a liquid epoxidation of 1-hexene with H2O2, ACS Omega (2020), <https://doi.org/10.1021/acsomega.0c00184>.
- [39] X. Fang, L. Sun, L. Lin, L. Wu, Y. Liu, Enhanced catalytic oxidation performance of F-Ti-MWW through the synergistic effect of anion and cation, Catal. Commun. 96 (2017) 54–57, <https://doi.org/10.1016/j.catcom.2017.04.007>.
- [40] K. Tang, W. Hou, X. Wang, W. Xu, X. Lu, R. Ma, Y. Fu, W. Zhu, Enhanced catalytic performance of trimethylsilylated Ti-MWW zeolites for the liquid-phase epoxidation of propylene with H2O2, Microporous Mesoporous Mater. 328 (2021) 111492, <https://doi.org/10.1016/J.MICROMESO.2021.111492>.

- [41] Y. Liu, Z. Tang, Y. Yu, W. Liu, Zhen Chen, R. Wang, H. Liu, H.-H. Wu, M.Y. He, Deboronation-assisted construction of defective Ti(OSi)₃OH species in MWW-type titanosilicate and their enhanced catalytic performance, *Catal. Sci. Technol.* (2020), <https://doi.org/10.1039/D0CY00126K>.
- [42] D.T. Bregante, J.Z. Tan, A. Sutrisno, D.W. Flaherty, Heteroatom substituted zeolite FAU with ultralow Al contents for liquid-phase oxidation catalysis, *Catal. Sci. Technol.* 10 (2020) 635–647, <https://doi.org/10.1039/c9cy01886g>.
- [43] J.Z. Tan, D.T. Bregante, C. Torres, D.W. Flaherty, Transition state stabilization depends on solvent identity, pore size, and hydrophilicity for epoxidations in zeolites, *J. Catal.* 405 (2022) 91–104, <https://doi.org/10.1016/J.JCAT.2021.11.029>.
- [44] D.T. Bregante, J.Z. Tan, R.L. Schultz, E.Z. Ayla, D.S. Potts, C. Torres, D.W. Flaherty, Catalytic consequences of oxidant, alkene, and pore structures on alkene epoxidations within titanium silicates, *ACS Catal.* 10 (2020) 10169–10184, <https://doi.org/10.1021/acscatal.0c02183>.
- [45] D.S. Potts, C. Torres, O. Kwon, D.W. Flaherty, Engineering intraporous solvent environments: effects of aqueous-organic solvent mixtures on competition between zeolite-catalyzed epoxidation and H₂O₂ decomposition pathways, *Chem. Sci.* 14 (2023) 3160–3181, <https://doi.org/10.1039/d2sc06473a>.
- [46] N. Liu, Y. Liu, W. Xie, L. Wang, M. He, P. Wu Hydrothermal synthesis of boron-free Ti-MWW with dual structure-directing agents Elsevier Inc , *Stud. Surf. Sci. Catal.*, 2007, 464–469, 10.1016/S0167-2991(07)80877-9.
- [47] P. Wu, T. Tatsumi, T. Komatsu, T. Yashima, A novel titanosilicate with MWW structure. I. Hydrothermal synthesis, elimination of extraframework titanium, and characterizations, *J. Phys. Chem. B* 105 (2001) 2897–2905, <https://doi.org/10.1021/jp002816s>.
- [48] X. Ouyang, Y.J. Wang Lee, S.J. Hwang, D. Xie, T. Rea, S.I. Zones, A. Katz, Novel surfactant-free route to delaminated all-silica and titanosilicate zeolites derived from a layered borosilicate MWW precursor, *Dalt. Trans.* 43 (2014) 10417–10429, <https://doi.org/10.1039/c4dt00383g>.
- [49] M. Moliner, A. Corma, Synthesis of expanded titanosilicate MWW-related materials from a pure silica precursor, *Chem. Mater.* 24 (2012) 4371–4375, <https://doi.org/10.1021/cm302509m>.
- [50] D.T. Bregante, D.S. Potts, O. Kwon, E.Z. Ayla, J.Z. Tan, D.W. Flaherty, Effects of hydrofluoric acid concentration on the density of silanol groups and water adsorption in hydrothermally synthesized transition-metal-substituted silicalite-1, *Chem. Mater.* 32 (2020) 7425–7437, <https://doi.org/10.1021/acs.chemmater.0c02405>.
- [51] T. Blasco, M.A. Camblor, A. Corma, P. Esteve, J.M. Guil, A. Martínez, J. Perdigón-Melón, S. Valencia, Direct synthesis and characterization of hydrophobic aluminum-free Ti-beta zeolite, *J. Phys. Chem. B* 102 (1998) 75–88, <https://doi.org/10.1021/jp973288w>.
- [52] J. Chen, L. Eberlein, C.H. Langford, Pathways of phenol and benzene photooxidation using TiO₂ supported on a zeolite, *J. Photochem. Photobiol. A Chem.* 148 (2002) 183–189, [https://doi.org/10.1016/S1010-6030\(02\)00041-2](https://doi.org/10.1016/S1010-6030(02)00041-2).
- [53] E.Z. Ayla, D.S. Potts, D.T. Bregante, D.W. Flaherty, Alkene epoxidations with H₂O₂ over groups 4–6 metal-substituted BEA zeolites: reactive intermediates, reaction pathways, and linear free-energy relationships, *ACS Catal.* 11 (2021) 139–154, <https://doi.org/10.1021/acscatal.0c03394>.
- [54] M.B. Sayed, R.A. Kydd, R.P. Cooney, A Fourier-transform infrared spectral study of H-ZSM-5 surface sites and reactivity sequences in methanol conversion, *J. Catal.* 88 (1984) 137–149, [https://doi.org/10.1016/0021-9517\(84\)90059-9](https://doi.org/10.1016/0021-9517(84)90059-9).
- [55] M. Shamzhy, B. Gil, M. Opanasenko, W.J. Roth, J. Čejka, MWW and MFI frameworks as model layered zeolites: structures, transformations, properties, and activity, *ACS Catal.* 11 (2021) 2366–2396, https://doi.org/10.1021/ACSCATAL.0C05332/ASSET/IMAGES/LARGE/CS0C05332_0011.JPG.
- [56] P. Wolf, C. Hammond, S. Conrad, I. Hermans, Post-synthetic preparation of Sn-, Ti- and Zr-beta: a facile route to water tolerant, highly active Lewis acidic zeolites, *Dalt. Trans.* 43 (2014) 4514–4519, <https://doi.org/10.1039/c3dt52972j>.
- [57] X. Ji, Y. Wang, T. Fujii, R. Otomo, J.N. Kondo, T. Yokoi, Evaluation of Ti distribution in zeolite framework based on the catalytic activity for alkene epoxidation, *Chem. Lett.* 48 (2019) 1130–1133, <https://doi.org/10.1246/cl.190387>.
- [58] D.T. Bregante, N.E. Thornburg, J.M. Notestein, D.W. Flaherty, Consequences of confinement for alkene epoxidation with hydrogen peroxide on highly dispersed group 4 and 5 metal oxide catalysts, *ACS Catal.* 8 (2018) 2995–3010, <https://doi.org/10.1021/acscatal.7b03986>.
- [59] D.T. Bregante, P. Priyadarshini, D.W. Flaherty, Kinetic and spectroscopic evidence for reaction pathways and intermediates for olefin epoxidation on Nb in *BEA, *J. Catal.* 348 (2017) 75–89, <https://doi.org/10.1016/j.jcat.2017.02.008>.
- [60] M.M.J. Treacy, J.M. Newsam, Two new three-dimensional twelve-ring zeolite frameworks of which zeolite beta is a disordered intergrowth, *Nature* 332 (1988) 249–251, <https://doi.org/10.1038/332249a0>.
- [61] E.L. First, C.E. Gounaris, J. Wei, C.A. Floudas, Computational characterization of zeolite porous networks: an automated approach, *Phys. Chem. Chem. Phys.* 13 (2011) 17339–17358, <https://doi.org/10.1039/C1CP21731C>.